NANO LETTERS

Letter

pubs.acs.org/NanoLett

Optimization of the Thermoelectric Figure of Merit in Crystalline C_{60} with Intercalation Chemistry

Jeong Yun Kim and Jeffrey C. Grossman*

Department of Materials Science and Engineering, Massachusetts Institute of Technology, Cambridge, Massachusetts 02139, United States

Supporting Information

ABSTRACT: Crystalline C_{60} is an appealing candidate material for thermoelectric (TE) applications due to its extremely low thermal conductivity and potentially high electrical conductivity with metal atom intercalation. We investigate the TE properties of crystalline C_{60} intercalated with alkali and alkaline earth metals using both classical and quantum mechanical calculations. For the electronic structure, our results show that variation of intercalated metal atoms has a large impact on energy dispersions, which leads to broad tunability of the power factor. For the thermal transport, we show that dopants introduce strong phonon scattering into crystalline C_{60}, leading to considerably lower thermal conductivity. Taking both into account, our calculations suggest that appropriate choice of metal atom intercalation in crystalline C_{60} could yield figures of merit near 1 at room temperature.

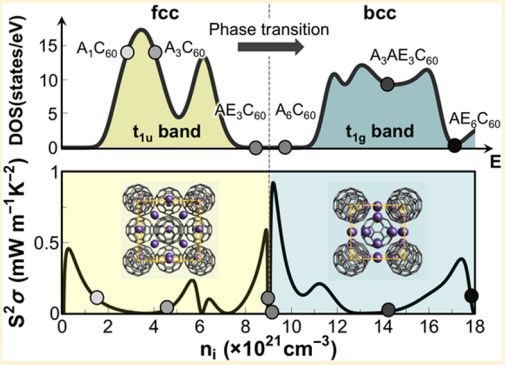

KEYWORDS: *Crystalline C_{60}, intercalation chemistry, organic thermoelectric materials, charge transport, thermal transport*

There is a growing interest in developing organic thermoelectric (TE) materials owing to their flexibility, low cost, and straightforward processing, offering new opportunities for flexible thermoelectric devices. Organic materials exhibit a naturally low thermal conductivity (κ) because of the weak bonding between constituents, which enhances the thermoelectric conversion efficiency as determined by its figure of merit, $ZT = S^2\sigma T/(\kappa_e + \kappa_l)$, where S is the Seebeck coefficient, σ the electrical conductivity, T the absolute temperature, κ_e the electronic thermal conductivity, and κ_l the lattice thermal conductivity. Recent experimental studies show great progress in organic TE materials, especially p-type polymers, with the highest ZT reported to be 0.42 at room temperature.[1−3] The majority of organic TE materials reported to date are based on p-type conductive polymers, such as poly(3,4-ethylenedioxythiophene) polystyrenesulfonate (PEDOT:PSS), whose power factor ($S^2\sigma$) is maximized with optimization of carrier concentration and microscopic morphologies via chemical doping.[1,2,4] In contrast, small molecule structures, such as those based on a fullerene or pentacene molecule, have received less attention regarding their potential for thermoelectric applications, despite benefits such as lower thermal conductivity and ease of purification and crystallization.[4]

Here, we focus on C_{60} as a possible building block for bulk organic thermoelectric materials. Due to the relatively large diameter (~7 Å) of the C_{60} molecule, solid C_{60} contains voids that can accommodate small ions, atoms, or even molecules, which in turn can have a large impact on properties. For example, metal-atom intercalation can be employed to tune broadly both thermal and electronic transport in crystalline C_{60} due to modification of the electronic structure, phonon modes, and conformation of the host molecular crystal itself.

Since the discovery of superconductivity in potassium-doped crystalline C_{60},[5] much attention has been given to understanding the role of dopants in alkali-doped C_{60}. It is well-known that doping with larger alkali atoms gives rise to an increase in the superconducting transition temperature due to the lattice constant expansion of the crystal, which leads to a larger density of states at the Fermi level. In contrast, the thermoelectric properties of metal-doped C_{60} have received little attention, despite its potentially high electrical conductivity and low thermal conductivity (~0.4 W m^{-1} K^{-1}).[6] Recent measurements of $S^2\sigma$ in crystalline C_{60} samples with cesium carbonate (Cs_2CO_3) doping have yielded very low values (20−30 μW m^{-1} K^{-2}) due to low values of σ (~5 S cm^{-1}) at low carrier concentrations,[7,8] although a systematic investigation of optimal doping conditions is needed in order to maximize the power factor and determine the potential of C_{60} as an efficient thermoelectric material.

In this work, a combination of first-principles electronic structure calculations and the Boltzmann transport approach are used to determine the role of dopants on the electrical transport properties, including the electrical conductivity (σ), Seebeck coefficient (S), and electronic thermal conductivity (κ_e). In addition, the lattice thermal conductivity κ_l is computed

Received: March 11, 2016
Revised: June 18, 2016

DOI: 10.1021/acs.nanolett.6b01073
Nano Lett. XXXX, XXX, XXX−XXX

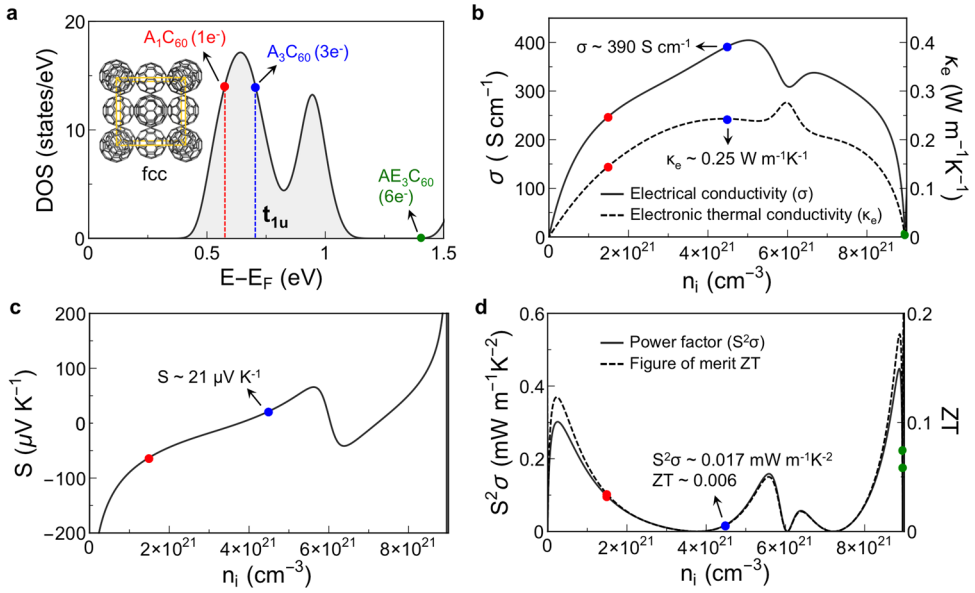

Figure 1. (a) Density of states (DOS) per unit cell of solid C_{60}. The red (blue and green) dot indicates the estimated Fermi level of A_1C_{60} (A_3C_{60} and AE_3C_{60}) sample, where 1 (3 and 6) electron is doped in the primitive fcc unit cell (A = alkali metal and AE = alkaline earth metal). Calculated electrical conductivity, electronic thermal conductivity (b), Seebeck coefficient (c), power factor and ZT values (d) of crystalline C_{60} as a function of doping concentration (n_i). Red (blue and green) dot shows thermoelectric properties of crystalline C_{60} at doping concentration corresponding to 1 (3 and 6) electron doping in the primitive unit cell. The Seebeck coefficient for the case of doping with 6 electrons (green dot) is not shown since the S value of this sample is beyond the range in panel c ($|S| \sim 500\ \mu V\ K^{-1}$).

using classical molecular dynamics simulations. Taken together, our results show that optimizing the type and concentration of doping in crystalline C_{60} can yield ZT $\sim$ 1.

Crystal and Electronic Structure of Crystalline C_{60}. In solid undoped C_{60}, face-centered cubic (fcc) packing is adopted with C_{60} molecules bonded via van der Waals interactions. The molecular states form Bloch states in the solid, with π-orbitals from the 5-fold degenerate molecular h_u levels forming the valence band, and the 3-fold degenerate t_{1u} molecular levels forming the conduction band. The lattice and electronic structure of solid C_{60} are calculated using density functional theory (DFT) as implemented in the plane-wave basis VASP code.[9] We used the projected augmented wave pseudopotentials[10] with the Ceperley-Alder exchange-correlation potential in the local density approximation (LDA).[11] For fulleride samples, we first used experimentally determined C and metal positions and optimized the geometry by using the conjugate gradient scheme until force components on every atom are less than 0.01 eV $Å^{-1}$. The fully relaxed structures are used to compute the electronic band structure. Our computed equilibrium lattice constant for fcc-C_{60} is 13.9 Å, in reasonable agreement with the experimental value of 14.13 Å.[12] The voids in the crystal can accommodate a host of impurity atoms, such as alkali metals, which in turn play an important role in the electronic properties of the solid, providing a wide range of accessible electronic states.

Thermoelectric Properties of Crystalline C_{60}. We first investigate the effect of doping on thermoelectric properties (σ, κ_e, and S) of crystalline C_{60} by employing semiclassical Boltzmann theory within the constant relaxation time approximation, as implemented in the BOLTZTRAP code.[13,14] The electrical conductivity, Seebeck coefficient, and electronic thermal conductivity are calculated through $\sigma = L^{(0)}$, $S = -1/eT\ (L^{(0)})^{-1}L^{(1)}$, and $\kappa_e = 1/e^2T(L^{(2)} - L^{(1)}(L^{(0)})^{-1}L^{(1)})$, where $L^{(\alpha)}$ is defined as

$$L^{(\alpha)} = e^2 \sum_n \int \frac{d\mathbf{k}}{4\pi^3} \tau_n(\varepsilon_n(\mathbf{k}))v_n(\mathbf{k})v_n(\mathbf{k})(\varepsilon_n(\mathbf{k}) - \mu)^\alpha \times \left(-\frac{\partial f}{\partial \varepsilon}\right)_{\varepsilon=\varepsilon_n(\mathbf{k})} \quad (1)$$

Here, e is the electronic charge, τ_n the energy-dependent relaxation time, $v_n(\mathbf{k}) = (1/\hbar)\nabla_{\mathbf{k}}\varepsilon_n(\mathbf{k})$ the group velocity in the nth band at $\mathbf{k}$, $\varepsilon_n(\mathbf{k})$ the energy eigenvalues obtained from DFT, μ the chemical potential, and f the Fermi–Dirac function at a given temperature T. The converged values of σ, S, and κ_e are obtained using a dense k-point mesh of 21 × 21 × 21 points. All simulations are carried out at 300 K and a carrier concentration range of $0–10^{22}$ cm^{-3}.

In order to predict accurate transport coefficients over a wide range of doping concentrations, we computed the energy-dependent relaxation time (τ), generally depending on the density of states ($N(\varepsilon)$). The charge transport in solid C_{60} can be determined by different types of carrier scattering processes. One of the most important scattering mechanism near room temperature is electron–phonon scattering, resulting in a linear temperature dependence of the resistivity.[15,16] Two other sources of scattering are the electron–electron scattering, leading to the presence of T^2-like dependence, and the scattering originated from orientational disorder, resulting in a large residual resistivity.[15,17] Accordingly, the overall relaxation time can be determined through

$$\frac{1}{\tau_{total}} = \frac{1}{\tau_0} + \frac{1}{\tau_{e-e}} + \frac{1}{\tau_{e-phonon}} \quad (2)$$

where $1/\tau_0$($1/\tau_{e-e}$ and $1/\tau_{e-phonon}$) is the scattering rate arising from orientational disorder (electron–electron and electron–phonon scattering, respectively). Here, all three terms are proportional to $N(\varepsilon)$, and accordingly the total scattering rate

DOI: 10.1021/acs.nanolett.6b01073
Nano Lett. XXXX, XXX, XXX–XXX

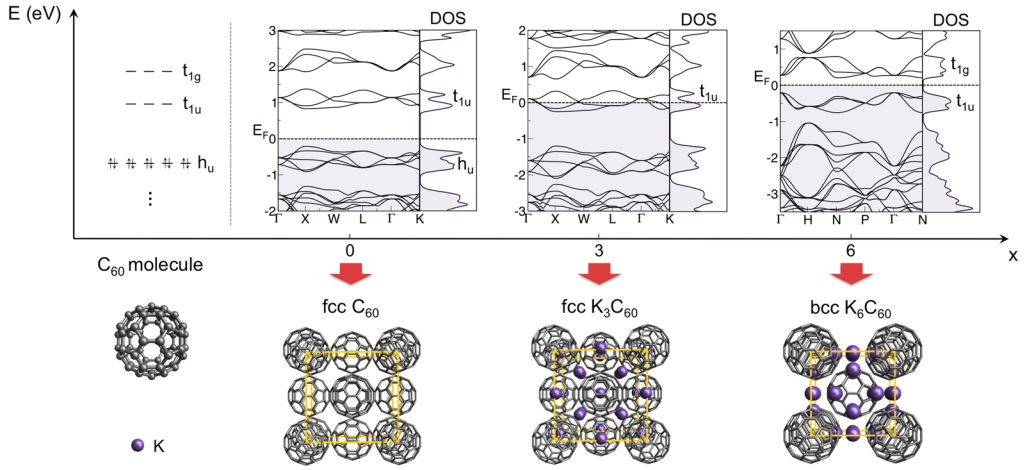

Figure 2. Electronic band structures and density of states (DOS) per unit cell of K_xC_{60} samples as a function of doping concentration (x) (upper). Discrete energy levels of isolated C_{60} molecule are shown at the left side of the graph. The unit cell of K_xC_{60} samples at each doping concentration (x = 0, 3, and 6) (lower). C and intercalated K atoms are represented by gray and purple spheres, respectively, and the yellow box represents the cubic unit cell of K_xC_{60}. Energy bands derived from the h_u, t_{1u}, and t_{1g} energy levels of C_{60} molecules are shown.

can be expressed as $1/\tau_{total}(\varepsilon) = A \times N(\varepsilon)$, where $A = 5.68 \times 10^{13}$ eV s^{-1} (see Supporting Information).

For calculations of the thermal transport, we perform equilibrium molecular dynamics (MD) simulations employed within the LAMMPS package.[18] The lattice thermal conductivity (κ_l) is computed from the fluctuations of the heat current, using the Einstein relation (see Supporting Information).[19−21] To describe the covalent bonding interactions between C atoms and the long-range van der Waals interactions for C, K, and C − K, we used the Goddard force field (GFF),[12,22] which has been successfully applied to the study of K-intercalated fullerenes.[23] All simulations are carried out at 300 K with a time step of 0.2 fs. To obtain converged results, 15 separate simulations are averaged for each system, each with different uncorrelated starting configurations. In each run, after a 200 ps equilibration period, the microscopic heat flux is recorded for 2×10^7 MD steps (4 ns) in order to obtain a converged thermal conductivity value. On the basis of convergence tests, we choose the size of the C_{60} lattice to be 40 Å (corresponding to 4000 atoms in the simulation cell) for all subsequent simulations. The lattice constants optimized with this force field are a = 14.13 and 14.18 Å for C_{60} and K_3C_{60}, respectively, which have the fcc crystal structure, and a = 11.39 Å for K_6C_{60} which has the bcc crystal structure. We used these values as fixed lattice parameters during the MD simulations.

In this work, we focus only on n-type doping, where the Fermi level lies within the t_{1u}-band (see Figure 1a). The electrical conductivity, electronic thermal conductivity, and Seebeck coefficient are computed as a function of carrier concentration (n_i) at room temperature (see Figure 1b and c). By combining these properties with our computed lattice thermal conductivity ($\kappa_l \sim 0.7$ W m^{-1} K^{-1}), the power factor, and ZT of solid C_{60} as a function of doping concentration are predicted in Figure 1d, showing several peak values within the doping range $n_i < 9 \times 10^{21}$ cm^{-3} (corresponding to doping with six electrons in the primitive unit cell, the maximum number of electrons that can be occupied in the t_{1u} band). Our computed $S^2\sigma$ for solid C_{60} without doping is 0.006 mW m^{-1} K^{-2} (corresponding to ZT ∼ 0.002) at room temperature. When solid C_{60} is doped with three alkali metals (A) in the primitive unit cell, the doping concentration is $n_i \sim 4.48 \times 10^{21}$ cm^{-3}, and $S^2\sigma$ at this doping concentration is 0.017 mW m^{-1} K^{-2} (corresponding to ZT ∼ 0.006). These estimated thermoelectric properties of A_3C_{60} are in good agreement with experimental measurements for K_3C_{60}.[16,17] The peaks in $S^2\sigma$ are achieved with doping concentrations $n_i \sim 2.3 \times 10^{20}$ cm^{-3} and 8.9×10^{21} cm^{-3}, corresponding to the bottom and top of the t_{1u} band edge, resulting in ZT ∼ 0.12 and 0.18, respectively. These results illustrate the usefulness of quantum mechanical calculations for predicting thermoelectric properties of solid C_{60} over a wide range of doping concentrations, and in turn predict optimal doping concentrations that maximize $S^2\sigma$. Next, we investigate the effects of intercalated dopants on the thermoelectric properties of solid C_{60}, with the aim of understanding the interplay between doping concentration, structural and electron structure changes, and the corresponding impact on TE properties.

Crystal and Electronic Structure of Alkali Metal-Doped C_{60}. The presence of alkali metal atoms at interstitial sites donates electrons to the t_{1u}-derived conduction band (or higher energy t_{1g}-band), depending on doping concentration. In the case of A_3C_{60}, the t_{1u} band is half-filled and metallic behavior is observed.[5] Further doping of metal atoms gives rise to a change of the C_{60} lattice structure from closed-packed fcc to a more open, body-centered lattice (bcc), with six equivalent distorted tetrahedral sites per C_{60}. The K_6C_{60} compounds are insulators as the t_{1u}-band is completely filled. Figure 2 shows the crystal structures and electronic band structures of C_{60}, K_3C_{60}, and K_6C_{60}, computed within DFT. Our results show these different behaviors, with K_3C_{60} metallic and K_6C_{60} possessing an indirect gap (Γ → N) of 0.5 eV, in good agreement with previous work.[24] In this work, we examine these two different compositions, fcc-A_3C_{60} and bcc-A_6C_{60}, and consider a range of combinations of alkali metals and alkaline earth elements as dopants.

Thermoelectric Properties of K_xC_{60}. We use K_xC_{60} as a model to investigate the effects of metal intercalation concentration on thermoelectric properties. Among three different K doping concentrations (x = 0, 3, and 6) in the primitive C_{60} unit cell, we predict both the intrinsic and maximum power factor ($S^2\sigma$), corresponding to the intrinsic and optimal doping levels, respectively (see Figure 3a). The maximum $S^2\sigma$ values are achieved at the edge of the t_{1u}-band for undoped C_{60} and K_3C_{60}, and the edge of the t_{1g}-band for K_6C_{60},

DOI: 10.1021/acs.nanolett.6b01073
Nano Lett. XXXX, XXX, XXX−XXX

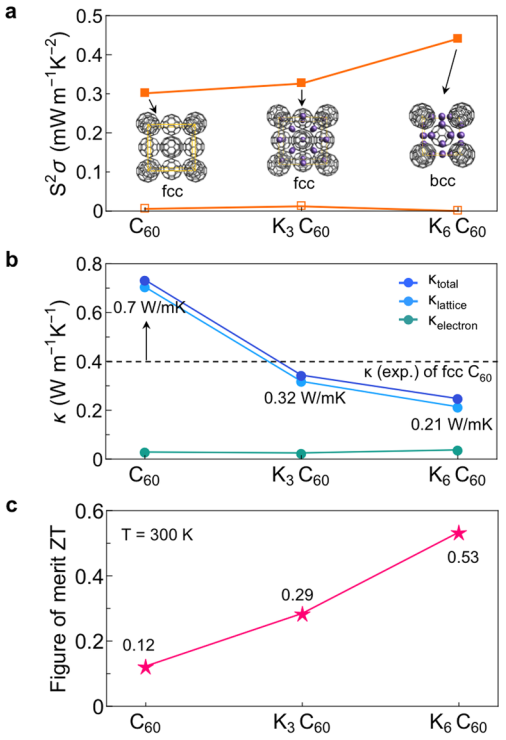

Figure 3. (a) Calculated power factors of C_{60}, K_3C_{60}, and K_6C_{60} at optimal doping (filled square) and intrinsic doping (empty square) concentrations. C_{60} and K_3C_{60} are in an fcc lattice, and K_6C_{60} is in a bcc lattice. (b) Calculated electronic (green), lattice (light blue), and total (dark blue) thermal conductivities of K_xC_{60} samples as a function of doping composition. Labels indicate computed lattice thermal conductivity values in each doping composition. The horizontal dashed line indicates the measured thermal conductivity of fcc-C_{60} ($\kappa \sim 0.4$ W m^{-1} K^{-1}).[6] (c) Figure of merit ZT at room temperature.

and increase by 2−3 orders of magnitude compared to the intrinsic values (see Supporting Information).

Figure 3b shows our computed κ_l for fcc-C_{60}, K_3C_{60}, and K_6C_{60} using classical molecular dynamics (MD) simulations. We note that the use of the Goddard force field[12,22] tends to overestimate κ_l with respect to the measured value for single crystal C_{60} (0.7 vs 0.4 W m^{-1} K^{-1} at 300 K in our calculations and experiment, respectively).[6] The low κ_l value is mainly due to a combination of ineffective heat transport across the weak van der Waals interactions linking C_{60} molecules and phonon scattering arising from the orientational disorder of C_{60} at room temperature.[6] The intercalation of K atoms suppresses κ_l, showing more than a 2-fold reduction from that of undoped C_{60} due to the disorder introduced by the rattling K atoms, enabling effective point-defect phonon scattering. Further doping of K atoms gives rise to further suppressed thermal transport, with κ_l = 0.21 W m^{-1} K^{-1} for K_6C_{60}, due to the higher density of rattling atoms in the unit cell. The κ_e values within the range we are interested are smaller than κ_l by an order of magnitude, as can be seen in Figure 3b. The total thermal conductivity (κ) is given as the sum of the electronic (κ_e) and lattice (κ_l) contributions, with the lowest κ value for K_6C_{60} in the bcc lattice.

Combining both the thermal and charge transport studies described above, we are able to predict the full ZT in K_xC_{60} samples at room temperature. Among the three fulleride samples, K_6C_{60} yields the highest ZT ∼ 0.53 at room temperature, owing to both the lowest κ and highest $S^2\sigma$. This high ZT value, compared with other organic TE materials, suggests the potential of alkali metal-doped C_{60} in the bcc lattice as a candidate material for thermoelectric applications. Here, it should be noted that our predicted values of ZT for K_xC_{60} samples are underestimated possibly by a factor of 2, arising from the overestimated κ_l values from MD simulations. Further, our calculations suggest that the experimentally improved power factor of C_{60} with Cs_2CO_3 doping (∼20 μW m^{-1} K^{-2})[8] could still be improved by an order of magnitude with the ability to access the optimal doping level.

Face-Centered Cubic (fcc) Fullerides: A_3C_{60}. Next, we consider the effects of different dopant atoms on TE properties by comparing A_3C_{60} (A = alkali metals Na, K, Rb, and Cs). The lattice parameter of these materials varies with dopant, with larger lattice constants leading to weaker overlap between electronic states of C_{60} molecules, resulting in a less dispersive t_{1u} band and larger density of states.

Key electronic structure properties for A_3C_{60} are shown in Figure 4. The lattice parameter ranges from 13.7 Å (Na_3C_{60}) to 14.4 Å (Cs_3C_{60}), and A_3C_{60} samples with smaller lattice parameter show lower density of states of the t_{1u}-band, expected to suppress S according to Mahan-Sofo theory.[25] In contrast, σ is expected to increase with decreasing lattice constant owing to more dispersive electronic bands. Our transport coefficient calculations confirm these trends as shown in Figure 4c−d. Between these two competing thermoelectric properties, σ is more influenced by the lattice variation than S, resulting in a maximum value of $S^2\sigma$ for the Na_3C_{60} sample (see Figure 4e). Although κ_e decreases with increasing lattice parameter as well, its role in our calculated ZT is negligible given the lower κ_e values by an order of magnitude compared to $S^2\sigma$.

In our calculations of ZT, we take the κ_l value for K_3C_{60} (0.32 W m^{-1} K^{-1}) for all of the A_3C_{60} samples since the variation in mass of the intercalated ion has a negligible effect on thermal transport. Among these samples, the Na_3C_{60} case exhibits the highest ZT ∼ 0.4 at room temperature, implying that a smaller lattice parameter is more favorable for thermoelectric applications, opposite to the case of C_{60}-based superconductivity.

Body-Centered Cubic (bcc) Fullerides: $A_{6-x}AE_xC_{60}$. We next consider the case of bcc fullerides, which possess lower κ_l compared to the fcc case. The charge transfer from an A ion to C_{60} is not complete in this lattice, resulting in a hybridization between the C_{60} and A electronic states.[24,26,27] Comparison between K_6C_{60} and hypothetical pristine bcc-C_{60} with the same lattice parameter demonstrates that the fully occupied t_{1u}-band of K_6C_{60} is considerably wider than that of the empty t_{1u}-band of pristine bcc-C_{60}, mainly due to the presence of hybridization between the C_{60} and K states (see Supporting Information).[26] In bcc fullerides, the electronic band becomes more dispersive with alkali metal doping, in contrast to the fcc case, where dispersion of the t_{1u} band is not affected by the potassium atom, but rather by the C_{60} overlap. Thus, unlike the fcc case where dopant variation serves primarily to modulate the lattice parameter, for bcc fullerides an additional degree of freedom arises due to hybridization. Here, we consider two different kinds of dopants, alkali metals (A_6C_{60}, A = Na, K, and Rb), alkaline earth metals (AE_6C_{60}, AE = Ca, Sr, and Ba, AE refers to alkaline earth metals) and their combinations ($K_3AE_3C_{60}$ and $A_3Ba_3C_{60}$), to investigate how doping influences the thermoelectric properties of bcc fullerides (see Figure 5b). We note that AE ions are expected to provide stronger hybridization

DOI: 10.1021/acs.nanolett.6b01073
Nano Lett. XXXX, XXX, XXX−XXX

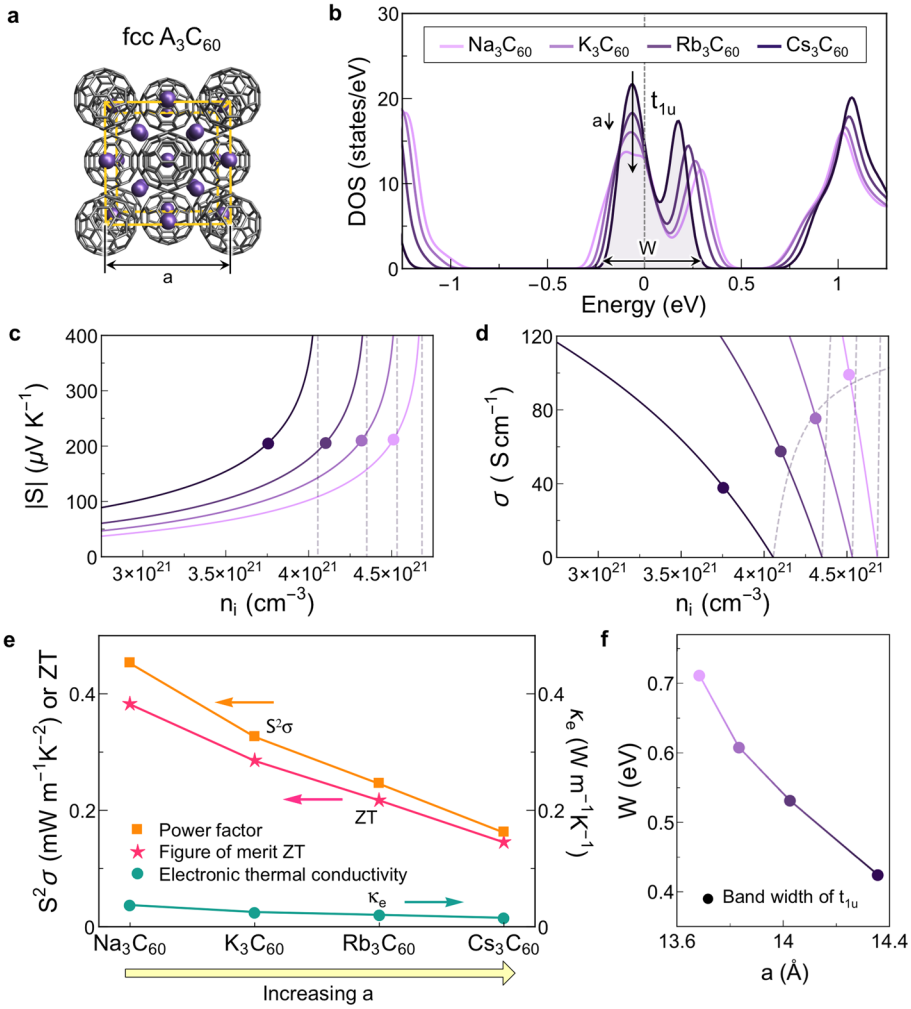

Figure 4. (a) Unit cell of fcc-A_3C_{60} sample along with structural variable used in the calculation. (b) Computed density of states of A_3C_{60} (A = Na, K, Rb, and Cs) fullerides. The lattice parameter of A_3C_{60} increases with the ionic radius of intercalated alkali metals. As the lattice parameter decreases, the density of states of the t_{1u} band in A_3C_{60} decreases. The bandwidth (W) of the t_{1u}-band is represented. (c, d) Seebeck coefficient (S) and electrical conductivity (σ) as a function of carrier concentrations (n_i). Dots indicate thermoelectric properties of each A_3C_{60} sample at optimal doping concentration that maximize ZT. (e) Electronic thermal conductivity (green), power factor (orange) and ZT (pink) for A_3C_{60} fullerides. These are the values at a given carrier concentration that exhibits maximum ZT values in each sample. (f) Calculated bandwidth (W) of the t_{1u}-band with corresponding lattice constant of A_3C_{60} samples.

between the C_{60} and ion states than A intercalation, leading to a wider bandwidth.[26]

As can be seen in Figure 5c, the t_{1g}-bandwidth of bcc $A_{6-x}AE_xC_{60}$ (x = 0, 3 and 6) fullerides decreases with lattice parameter within the samples with the same composition, similar to the fcc A_3C_{60} fulleride cases. However, samples with the same lattice parameter do not always result in the same bandwidth. Fulleride samples ($A_{6-x}AE_xC_{60}$) with higher AE ion composition (x) exhibit larger bandwidths than the samples with lower AE ion composition even with the same lattice parameter: W (x = 6) > W (x = 3) > W (x = 0). We note that this bandwidth gap arises from the different hybridization of each dopant, and stronger hybridization is generated with AE ions. This trend can be explained by the previous valence-electron density study of the $K_3Ba_3C_{60}$ fulleride,[26] demonstrating that considerable electron densities remain around both the Ba and K sites, with larger density around Ba compared to K, implying stronger hybridization with Ba ions.

Our calculated thermoelectric properties for $A_{6-x}AE_xC_{60}$ (x = 0, 3, 6) are shown in Figure 5d–f. As expected, σ increases with bandwidth, while S decreases, leading to a maximum in the power factor as a function of bandwidth at $W \sim 0.9$ eV for Ba_6C_{60}. Below this bandwidth, $S^2\sigma$ increases with W, as in the case of the fcc lattice, mostly due to the increase in σ. Significant $S^2\sigma$ reduction beyond its maximum point arises from considerably reduced S values, by a factor of 7, compared with other $A_{6-x}AE_xC_{60}$ samples, despite the increased σ values (see Supporting Information). This decrease in the Seebeck coefficient can be explained by the strong hybridization between C_{60} and AE states, inducing an overlap between valence and conduction bands that makes these fullerides semimetallic.[28] κ_e increases with bandwidth, owing to more dispersive electronic bands with larger bandwidth, as in the case of σ. These results demonstrate that the hybridization between C_{60} and dopant metal states plays an important role in the charge transport of crystalline C_{60} in the bcc lattice, and optimization of dopants could lead to further improvement of the electronic properties in crystalline C_{60}.

Combining these power factors with our computed lattice thermal conductivity of K_6C_{60} (κ_l = 0.21 W m^{-1} K^{-1}) allows us

DOI: 10.1021/acs.nanolett.6b01073
Nano Lett. XXXX, XXX, XXX−XXX

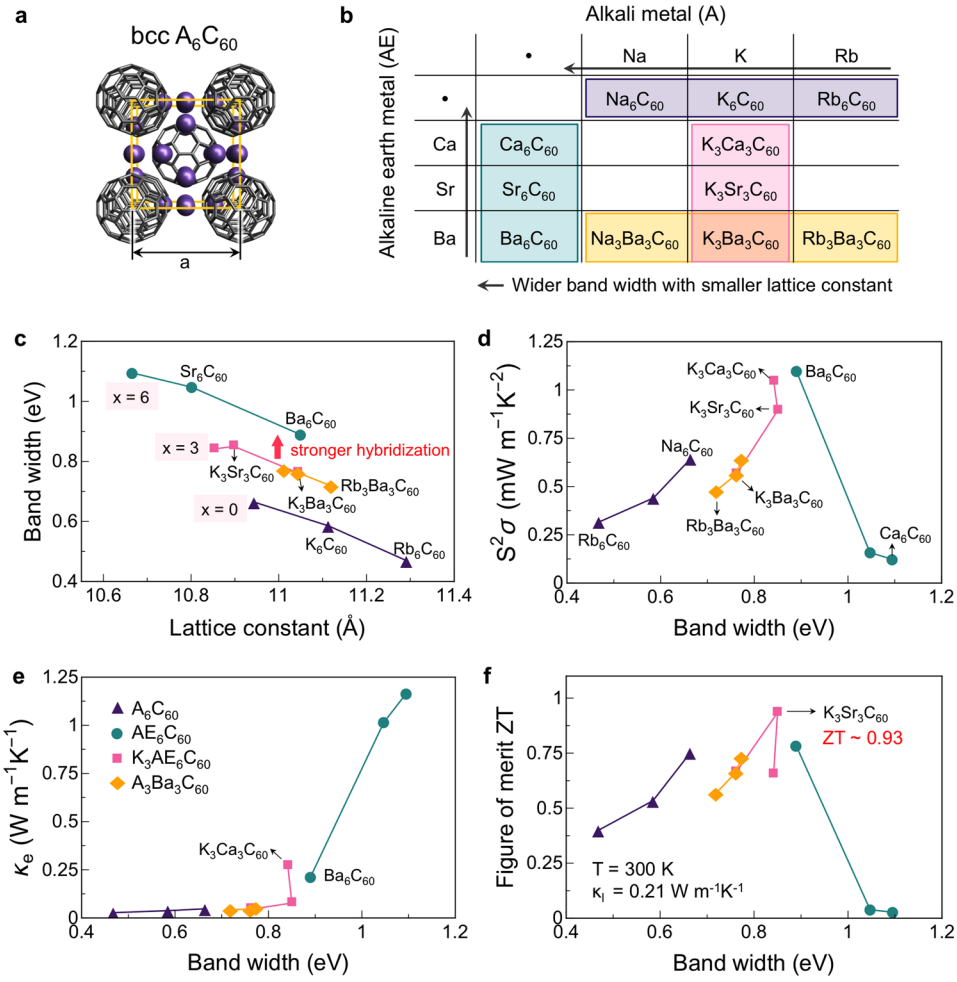

Figure 5. (a) Unit cell of bcc-A_6C_{60} sample along with structural variables. (b) All $A_{6-x}AE_xC_{60}$ (x = 0, 3, and 6) samples considered in this work are listed. We consider three different alkali metals (Na, K, and Rb) and three different alkali earth metals (Ca, Sr, and Ba). Arrows indicate the directions for bandwidth increase and lattice constant decrease. (c) Calculated bandwidth (W) of the t_{1g}-band with corresponding lattice constant of $A_{6-x}AE_xC_{60}$ samples. (d) Power factors, (e) electronic thermal conductivities, and (f) figure of merit ZT of bcc fullerides as a function of bandwidth (W).

to predict ZT for the bcc fullerides (Figure 5f). Among these samples, a ZT as large as 1 can be achieved in the case of $K_3Sr_3C_{60}$ at room temperature. These high theoretical ZT values (60 times higher than the maximum measured ZT ~ 0.015 for crystalline C_{60})[8] are achieved mainly due to a careful exploration of optimal doping conditions, with access to the optimal doping concentration giving an order of magnitude increase and optimizing the intercalation chemistry providing another factor of 7 according to our calculations. Significant ZT enhancement in the $K_3Sr_3C_{60}$ sample, by a factor of ~7 with respect to the crystalline C_{60} case, is due to a combination of a reduction in κ and enhancement in $S^2\sigma$. As we noted earlier, for solid C_{60} our computed lattice thermal conductivity is overestimated by a factor of 1.8 with respect to the measured value, which if taken into account implies that our computed ZT for the fullerides are underestimates. These results highlight the importance of optimizing intercalating dopants in crystalline C_{60} and show that suitable choices could lead to efficient TE by simultaneously improving the properties constituting ZT.

In this work, we investigated the thermoelectric properties of crystalline C_{60} intercalated with alkali and alkaline earth metals using both classical and quantum mechanical calculations. The intercalation of metal atoms plays an important role in controlling both thermal and charge transport. Introduction of dopants generates strong phonon scattering in crystalline C_{60}, and thermal transport in such materials can be tuned by dopant composition. These results also demonstrate that dopant variation broadly tailors the charge transport in fullerides, introducing different effects on the bandwidths, which play a dominant role in determining the charge transport in crystalline C_{60}. Our results suggest that tailored introduction of metal atoms in crystalline C_{60} could be an important route to designing high-efficiency fullerene-based thermoelectric materials.

■ ASSOCIATED CONTENT

Supporting Information

The Supporting Information is available free of charge on the ACS Publications website at DOI: 10.1021/acs.nanolett.6b01073.

Additional simulation details on thermal conductivity (molecular dynamics simulations), electronic structure (quantum mechanical simulations), and relaxation time calculations. Optimal doping levels of fullerides samples (PDF)

DOI: 10.1021/acs.nanolett.6b01073
Nano Lett. XXXX, XXX, XXX−XXX

AUTHOR INFORMATION

Corresponding Author

*E-mail: jcg@mit.edu.

Notes

The authors declare no competing financial interest.

ACKNOWLEDGMENTS

This research used resources of the National Energy Research Scientific Computing Center, a DOE Office of Science User Facility supported by the Office of Science of the U.S. Department of Energy under Contract No. DE-AC02-05CH11231. This work was partially supported by the Eni Solar Frontiers Center at MIT.

REFERENCES

(1) Bubnova, O.; Khan, Z. U.; Malti, A.; Braun, S.; Fahlman, M.; Berggren, M.; Crispin, X. *Nat. Mater.* **2011**, *10*, 429−433.
(2) Kim, G. H.; Shao, L.; Zhang, K.; Pipe, K. P. *Nat. Mater.* **2013**, *12*, 719−723.
(3) Wan, C. L.; Gu, X. K.; Dang, F.; Itoh, T.; Wang, Y. F.; Sasaki, H.; Kondo, M.; Koga, K.; Yabuki, K.; Snyder, G. J.; Yang, R. G.; Koumoto, K. *Nat. Mater.* **2015**, *14*, 622−627.
(4) Zhang, Q.; Sun, Y. M.; Xu, W.; Zhu, D. B. *Adv. Mater.* **2014**, *26*, 6829−6851.
(5) Haddon, R. C. *Acc. Chem. Res.* **1992**, *25*, 127−133.
(6) Yu, R. C.; Tea, N.; Salamon, M. B.; Lorents, D.; Malhotra, R. *Phys. Rev. Lett.* **1992**, *68*, 2050−2053.
(7) Barbot, A.; Di Bin, C.; Lucas, B.; Ratier, B.; Aldissi, M. *J. Mater. Sci.* **2013**, *48*, 2785−2789.
(8) Sumino, M.; Harada, K.; Ikeda, M.; Tanaka, S.; Miyazaki, K.; Adachi, C. *Appl. Phys. Lett.* **2011**, *99*, 093308.
(9) Kresse, G.; Furthmuller, J. *Phys. Rev. B: Condens. Matter Mater. Phys.* **1996**, *54*, 11169−11186.
(10) Kresse, G.; Joubert, D. *Phys. Rev. B: Condens. Matter Mater. Phys.* **1999**, *59*, 1758−1775.
(11) Ceperley, D. M.; Alder, B. J. *Phys. Rev. Lett.* **1980**, *45*, 566−569.
(12) Quo, Y. J.; Karasawa, N.; Goddard, W. A. *Nature* **1991**, *351*, 464−467.
(13) Madsen, G. K. H.; Singh, D. J. *Comput. Phys. Commun.* **2006**, *175*, 67−71.
(14) Kim, J. Y.; Grossman, J. C. *Nano Lett.* **2015**, *15*, 2830−2835.
(15) Crespi, V. H.; Hou, J. G.; Xiang, X.; Cohen, M. L.; Zettl, A. *Phys. Rev. B: Condens. Matter Mater. Phys.* **1992**, *46*, 12064−12067.
(16) Erwin, S. C.; Pickett, W. E. *Phys. Rev. B: Condens. Matter Mater. Phys.* **1992**, *46*, 14257−14260.
(17) Palstra, T. T. M.; Haddon, R. C.; Hebard, A. F.; Zaanen, J. *Phys. Rev. Lett.* **1992**, *68*, 1054−1057.
(18) Plimpton, S. *J. Comput. Phys.* **1995**, *117*, 1−19.
(19) Weitz, D. A.; Pine, D. J.; Pusey, P. N.; Tough, R. J. A. *Phys. Rev. Lett.* **1989**, *63*, 1747−1750.
(20) Viscardy, S.; Servantie, J.; Gaspard, P. *J. Chem. Phys.* **2007**, *126*, 184513.
(21) Kim, J. Y.; Lee, J. H.; Grossman, J. C. *ACS Nano* **2012**, *6*, 9050−9057.
(22) Chen, G. H.; Guo, Y. J.; Karasawa, N.; Goddard, W. A. *Phys. Rev. B: Condens. Matter Mater. Phys.* **1993**, *48*, 13959−13970.
(23) Gao, G. H.; Cagin, T.; Goddard, W. A. *Phys. Rev. Lett.* **1998**, *80*, 5556−5559.
(24) Erwin, S. C.; Pederson, M. R. *Phys. Rev. Lett.* **1991**, *67*, 1610−1613.
(25) Mahan, G. D.; Sofo, J. O. *Proc. Natl. Acad. Sci. U. S. A.* **1996**, *93*, 7436−7439.
(26) Umemoto, K.; Saito, S.; Oshiyama, A. *Phys. Rev. B: Condens. Matter Mater. Phys.* **1999**, *60*, 16186−16191.
(27) Erwin, S. C.; Pederson, M. R. *Phys. Rev. B: Condens. Matter Mater. Phys.* **1993**, *47*, 14657−14660.
(28) Kortan, A. R.; Kopylov, N.; Glarum, S.; Gyorgy, E. M.; Ramirez, A. P.; Fleming, R. M.; Zhou, O.; Thiel, F. A.; Trevor, P. L.; Haddon, R. C. *Nature* **1992**, *360*, 566−568.

DOI: 10.1021/acs.nanolett.6b01073
Nano Lett. XXXX, XXX, XXX−XXX